Research Article | Vol. 24, No. 16 | 8 Aug 2016 | OPTICS EXPRESS 18525

Optics EXPRESS

Mapping the energy density of shaped waves in scattering media onto a complete set of diffusion modes

OLUWAFEMI S. OJAMBATI,[1,*] ALLARD P. MOSK,[1] IVO M. VELLEKOOP,[2] AD LAGENDIJK,[1] AND WILLEM L. VOS[1]

[1]*Complex Photonic Systems (COPS), MESA+ Institute for Nanotechnology, University of Twente, PO Box 217, 7500 AE Enschede, The Netherlands*
[2]*MIRA Institute for Biomedical Technology and Technical Medicine, University of Twente, PO Box 217, 7500 AE Enschede, The Netherlands*
[*]*o.s.ojambati@utwente.nl*

Abstract: We study the energy density of shaped waves inside a quasi-1D disordered waveguide. We find that the spatial energy density of optimally shaped waves, when expanded in the complete set of eigenfunctions of the diffusion equation, is well described by considering only a few of the lowest eigenfunctions. Taking into account only the fundamental eigenfunction, the total internal energy inside the sample is underestimated by only 2%. The spatial distribution of the shaped energy density is very similar to the fundamental eigenfunction, up to a cosine distance of about 0.01. We obtain the energy density of transmission eigenchannels inside the sample by numerical simulation of the scattering matrix. Computing the transmission-averaged energy density over all transmission channels yields the ensemble averaged energy density of shaped waves. From the averaged energy density, we reconstruct its spatial distribution using the eigenfunctions of the diffusion equation. The results of our study have exciting applications in controlled biomedical imaging, efficient light harvesting in solar cells, enhanced energy conversion in solid-state lighting, and low threshold random lasers.

OCIS codes: (290.1990) Diffusion; (290.4210) Multiple scattering; (290.7050) Turbid media.

References and links

1. J. W. Goodman, *Statistical Optics* (Wiley, 2000).
2. A. Ishimaru, *Wave Propagation and Scattering in Random Media* (Academic, 1978).
3. M. C. W. van Rossum and Th. M. Niewenhuizen, "Multiple scattering of classical waves," Rev. Mod. Phys. **71**, 313–371 (1999).
4. E. Akkermans and G. Montambaux, *Mesoscopic Physics of Electrons and Photons* (Cambridge University, 2007).
5. I. Freund, "Looking through walls and around corners," Physica A **168**(1), 49 – 65 (1990).
6. I. M. Vellekoop and A. P. Mosk, "Focusing coherent light through opaque strongly scattering media," Opt. Lett. **32**, 2309–2311 (2007).
7. I. M. Vellekoop and A. P. Mosk, "Universal optimal transmission of light through disordered materials," Phys. Rev. Lett. **101**, 120601 (2008).
8. M. Davy, Z. Shi, and A. Z. Genack, "Focusing through random media: Eigenchannel participation number and intensity correlation," Phys. Rev. B **85**, 035105, (2012).
9. A. P. Mosk, A. Lagendijk, G. Lerosey, and M. Fink, "Controlling waves in space and time for imaging and focusing in complex media," Nature Photon. **6**, 283–292 (2012).
10. S. M. Popoff, A. Goetschy, S. F. Liew, A. D. Stone, and H. Cao, "Coherent control of total transmission of light through disordered media," Phys. Rev. Lett. **112**, 133903 (2014).
11. I. M. Vellekoop, "Feedback-based wavefront shaping," Opt. Express **23**, 12189–12206 (2015).
12. A. Derode, P. Roux, and M. Fink, "Robust acoustic time reversal with high-order multiple scattering," Phys. Rev. Lett. **75**, 4206–4209 (1995).
13. G. Lerosey, J. de Rosny, A. Tourin, A. Derode, G. Montaldo, and M. Fink, "Time reversal of electromagnetic waves," Phys. Rev. Lett. **92**, 193904 (2004).
14. G. Lerosey, J. de Rosny, A. Tourin, and M. Fink, "Focusing beyond the diffraction limit with far-field time reversal," Science **315**, 1120–1122 (2007).
15. E. N. Leith and J. Upatnieks, "Holographic imagery through diffusing media," J. Opt. Soc. Am. **56**, 523–523 (1966).
16. D. R. Dowling and D. R. Jackson, "Narrow ÂŘband performance of phase ÂŘconjugate arrays in dynamic random media," J. Acoust. Soc. Am. **91**, 3257 (1992).

#263184 http://dx.doi.org/10.1364/OE.24.018525
Journal © 2016 Received 13 Apr 2016; revised 10 Jun 2016; accepted 5 Jul 2016; published 3 Aug 2016

Optics EXPRESS

17. Z. Yaqoob, D. Psaltis, M. S. Feld, and C. Yang, "Optical phase conjugation for turbidity suppression in biological samples," Nature Photon. **2**, 110–115 (2008).
18. S. M. Popoff, G. Lerosey, R. Carminati, M. Fink, A. C. Boccara, and S. Gigan, "Measuring the transmission matrix in optics: An approach to the study and control of light propagation in disordered media," Phys. Rev. Lett. **104**, 100601 (2010).
19. S. M. Popoff, G. Lerosey, M. Fink, A. C. Boccara, and S. Gigan, "Controlling light through optical disordered media: transmission matrix approach," New J. Phys. **13**, 123021 (2011).
20. M. Kim, Y. Choi, C. Yoon, W. Choi, J. Kim, Q.-H. Park, and W. Choi, "Maximal energy transport through disordered media with the implementation of transmission eigenchannels," Nature Photon. **6**, 581 (2012).
21. Y. M. Wang, B. Judkewitz, C. A. DiMarzio, and C. Yang, "Deep-tissue focal fluorescence imaging with digitally time-reversed ultrasound-encoded light," Nat. Commun. **3**, 928, (2012).
22. K. Si, R. Fiolka, and M. Cui, "Fluorescence imaging beyond the ballistic regime by ultrasound-pulse-guided digital phase conjugation," Nature Photon. **6**, 657–661 (2012).
23. J. Bertolotti, E. G. van Putten, C. Blum, A. Lagendijk, W. L. Vos, and A. P. Mosk, "Non-invasive imaging through opaque scattering layers," Nature **491**, 232–234, (2012).
24. T. Čižmar, M. Mazilu, and K. Dholakia, "In situ wavefront correction and its application to micromanipulation," Nature Photon. **4**, 388–394 (2010).
25. J.-H. Park, C. Park, H. Yu, Y.-H. Cho, and Y. Park, "Dynamic active wave plate using random nanoparticles," Opt. Express **20**, 17010–17016, (2012).
26. Y. Guan, O. Katz, E. Small, J. Zhou, and Y. Silberberg, "Polarization control of multiply scattered light through random media by wavefront shaping," Opt. Lett. **37**, 4663–4665 (2012).
27. J.-H. Park, C. Park, H. Yu, Y.-H. Cho, and Y. Park, "Active spectral filtering through turbid media," Opt. Lett. **37**, 3261–3263 (2012).
28. E. Small, O. Katz, Y. Guan, and Y. Silberberg, "Spectral control of broadband light through random media by wavefront shaping," Opt. Lett. **37**, 3429–3431 (2012).
29. S. R. Huisman, T. Huisman, T. A. W. Wolterink, A. P. Mosk, and P. W. H. Pinkse, "Programmable multiport optical circuits in opaque scattering materials," Opt. Express **23**(2), 3102–3116 (2015).
30. R. Horstmeyer, B. Judkewitz, I. M. Vellekoop, S. Assawaworrarit, and C. Yang, "Physical key-protected one-time pad," Sci. Rep. **3**, 3543 (2013).
31. S. A. Goorden, M. Horstmann, A. P. Mosk, B. Škoríc, and P. W. H. Pinkse, "Quantum-secure authentication of a physical unclonable key," Optica **1**, 421–424 (2014).
32. M. R. Krames, O. B. Shchekin, R. Mueller-Mach, G. O. Mueller, L. Zhou, G. Harbers, and M. G. Craford, "Status and future of high-power light-emitting diodes for solid-state lighting," J. Display Technol. **3**, 160–175 (2007).
33. J. M. Phillips, M. E. Coltrin, M. H. Crawford, A. J. Fischer, M. R. Krames, R. Mueller-Mach, G. O. Mueller, Y. Ohno, L. E. S. Rohwer, J. A. Simmons, and J. Y. Tsao, "Research challenges to ultra-efficient inorganic solid-state lighting," Laser Photon. Rev. **1**(4), 307–333 (2007).
34. V. Y. F. Leung, A. Lagendijk, T. W. Tukker, A. P. Mosk, W. L. IJzerman, and W. L. Vos, "Interplay between multiple scattering, emission, and absorption of light in the phosphor of a white light-emitting diode," Opt. Express **22**, 8190–8204, (2014).
35. T. Ogi, A. B. D. Nandiyanto, K. Okino, F. Iskandar, W.-N. Wang, E. Tanabe, and K. Okuyama, "Towards better phosphor design: Effect of SiO2 nanoparticles on photoluminescence enhancement of YAG:Ce," ECS J. Solid State Sci. Technol. **2**(5), R91–R95 (2013).
36. M. L. Meretska, A. Lagendijk, H. Thyrrestrup, A. P. Mosk, W. L. IJzerman, and W. L. Vos, "How to distinguish elastically scattered light from stokes shifted light for solid-state lighting?," J. Appl. Phys. **119**, 093102 (2016).
37. J. A. Levitt and W. H. Weber, "Materials for luminescent greenhouse solar collectors," Appl. Opt. **16**, 2684–2689 (1977).
38. A. Polman and H. Atwater, "Photonic design principles for ultrahigh-efficiency photovoltaics," Nature Mater. **11**, 174 (2012).
39. F. T. Si, D. Y. Kim, R. Santbergen, H. Tan, R. A. C. M. M. van Swaaij, A. H. M. Smets, O. Isabella, and M. Zeman, "Quadruple-junction thin-film silicon-based solar cells with high open-circuit voltage," Appl. Phys. Lett. **105**, 063902 (2014).
40. D. S. Wiersma and A. Lagendijk, "Light diffusion with gain and random lasers," Phys. Rev. E **54**, 4256–4265 (1996).
41. N. M. Lawandy, R. M. Balachandran, A. S. L. Gomes, and E. Sauvain, "Laser action in strongly scattering media," Nature **368**, 436 (1994).
42. O. Yizhar, L. E. Fenno, T. J. Davidson, M. Mogri, and K. Deisseroth, "Optogenetics in neural systems," Neuron **71**, 9–34 (2011).
43. W. Choi, A. P. Mosk, Q.-H. Park, and W. Choi, "Transmission eigenchannels in a disordered medium," Phys. Rev. B **83**, 134207 (2011).
44. M. Davy, Z. Shi, J. Park, C. Tian, and A. Z. Genack, "Universal structure of transmission eigenchannels inside opaque media," Nat. Commun. **6**, 6893 (2015).
45. S. F. Liew and H. Cao, "Modification of light transmission channels by inhomogeneous absorption in random media," Opt. Express **23**, 11043–11053 (2015).
46. B. Gérardin, J. Laurent, A. Derode, C. Prada, and A. Aubry, "Full transmission and reflection of waves propagating

Optics EXPRESS

through a maze of disorder," Phys. Rev. Lett. **113**, 173901 (2014).
47. O. S. Ojambati, H. Yılmaz, A. Lagendijk, A. P. Mosk, and W. L. Vos, "Coupling of energy into the fundamental diffusion mode of a complex nanophotonic medium," New J. Phys. **18**, 043032 (2016).
48. P. M. Morse and H. Feshbach, *Methods of Theoretical Physics* (McGraw-Hill., 1953).
49. K. F. Riley, M. P. Hobson, and S. J. Bence, *Mathematical Methods for Physics and Engineering* (Cambridge University, 2006).
50. P. Dennery, and A. Krzywicki, *Mathematics for Physicists* (Dover, 1967).
51. D. Y. K. Ko and J. C. Inkson, "Matrix method for tunneling in heterostructures: Resonant tunneling in multilayer systems," Phys. Rev. B **38**, 9945–9951 (1988).
52. J. B. Pendry and A. MacKinnon, "Calculation of photon dispersion relations," Phys. Rev. Lett. **69**, 2772–2775 (1992).
53. C. W. J. Beenakker, "Random-matrix theory of quantum transport," Rev. Mod. Phys. **69**, 731–808 (1997).
54. We note that in some other forms of the diffusion equation, the diffusion constant has dimensions differing from $[L]^2[T]^{-1}$.
55. A. Lagendijk, R. Vreeker, and P. de Vries, "Influence of internal reflection on diffusive transport in strongly scattering media," Phys. Lett. A **136**, 81–88 (1989).
56. The form of Eqs. 11 and 12 is different from the ones obtained in [55] because we have considered here the extrapolation lengths from both surfaces possibly to be different, while in [55] they were considered to be the same.
57. G. Salton and M. J. McGill, *Introduction to Modern Information Retrieval* (McGraw Hill, 1986).

1. Introduction

There are numerous scattering media that are either of natural origin - such as biological tissue, fog, cloud, and teeth - or man-made - such as paint, diffuser glass, and phosphor inclusions in white LEDs. These materials multiply scatter waves in all directions, due to the random spatial variations of the refractive indices. Random interference occurs between the multiply scattered waves that is well-known as speckles [1]. Upon averaging over realizations of scatterers, the speckles average out and the resulting average energy density is well described by diffusion theory [2–4].

Recently, novel wave-shaping methods such as feedback-based wavefront shaping [5–11], time reversal [12–14], phase conjugation [15–17], and transmission matrix-based control [18–20] have demonstrated the control of transmission and reflection through scattering media. These wave-shaping methods remarkably enhance the intensity in a single speckle as well as the total reflected and transmitted intensity. The wave-shaping methods have led the way for exciting applications such as non-invasive biomedical imaging [21–23], advanced optics [24–29], and cryptography and secure communication [30, 31].

Although these methods are useful tools in controlling the intensity at the interfaces of a scattering medium, the energy density distribution of the shaped waves inside the scattering medium is still unknown. Here, we refer to shaped waves to mean perfect phase conjugation of the transmitted waves, which is equivalent to shaping to optimally focus light to a single speckle spot [7, 11]. In the case of light, the knowledge of the energy density distribution is important for applications such as enhanced energy conversion in white LEDs [32–36], efficient light harvesting in solar cells [37–39], high yield random laser [40, 41], and controlled illumination in biomedical imaging [42]. To date, only numerical calculations of scalar waves [43–45] and a single-realization elastic wave experiment [46] have addressed the energy density distribution of shaped waves inside two-dimensional (2D) scattering media. However, none of these studies provide an analytical model for the energy density distribution. For high-transmission channels, Davy *et al* [44] described the energy density using a parabolic function. In [47], our team reported the first measurement of the total energy density of light inside a three-dimensional (3D) scattering medium and reported an enhanced total energy density for shaped waves. In that paper, the experimental result was interpreted with a model that describes the total energy density of shaped waves using only the fundamental eigenfunction of the diffusion equation. The model agreed well with experimental observation. However, the much wanted full description of the spatial energy density for shaped waves needs a more fundamental study.

In this paper, we examine the spatial energy density of shaped waves inside a scattering

Optics EXPRESS

medium. Our starting point is the mathematical theorem that the eigenfunctions of the diffusion equation form a complete set [48–50]. Therefore, this set can describe any function defined on the sample support, which is specified by the two boundaries. As an example, the complete set of diffusion eigenfunctions can accurately describe the spatial energy density as well as any speckle inside the sample. The fact that the diffusion eigenfunctions can describe any function inside the medium implies in no way a connection to the diffusion approximation. However, such a connection can be inferred if it turns out that the required number of eigenfunctions is small. In this paper, we will demonstrate that expanding the spatial energy density using the complete set of diffusion eigenfunctions is enlightening because only a few diffusion eigenfunctions suffice to reconstruct the energy density.

We obtained the spatial energy density inside a quasi-1D disordered waveguide by numerical calculation of concatenated scattering matrices [51–53]. A quasi-1D disordered waveguide provides a tractable platform to study the essential physics. We calculated the spatial energy density $W(z)$ of all transmission channels. By calculating the transmission-averaged energy density for all transmission channels, we retrieved the energy density of shaped waves [7, 11]. We obtained the intensity transmission coefficients of all channels, and we henceforth refer to τ as the transmission of a specific channel.

We show that only the first seven diffusion eigenfunctions suffice to reconstruct the spatial energy density distribution of the shaped waves. Taking into account only the fundamental eigenfunction of the diffusion equation, the total internal energy inside the sample is underestimated by only 2%. The spatial energy density is very similar to the fundamental eigenfunction, with a cosine distance of 0.01. Furthermore, we are able to reconstruct the energy density distribution of both high- and low- transmission channels, using a few M eigenfunctions of the diffusion equation, *e.g.* $M = 16$ for channels with transmission $\tau = 0.1$.

It is fascinating to see that the energy densities of shaped waves and transmission channels, which are due to interference effects, can be truly described using a few diffusion eigensolutions. The reconstruction of the distribution of the energy densities that we found here can be extended to three dimensional (3D) scattering samples. The reconstruction also applies to all forms of waves such as light, sound, elastic waves and quantum waves.

2. Theory

2.1. Eigenfunctions of the diffusion equation

The diffusion equation describes the ensemble averaged energy density $W(\mathbf{r}, t)$ of multiply scattered waves as a function of position $\mathbf{r}$ and time t inside a scattering medium [2, 3],

$$\frac{\partial W(\mathbf{r}, t)}{\partial t} = D\nabla^2 W(\mathbf{r}, t), \tag{1}$$

where D is the diffusion constant [54]. Anticipating the fact that the directions (x, y) are decoupled from the z-direction we decompose the energy density as

$$W(\mathbf{r}, t) = W_\perp(x, y, t)\, W(z, t)\,. \tag{2}$$

Since we are considering a slab that is a quasi-1D scattering medium, we assume statistical translational invariance in the perpendicular directions (x, y). The sample boundaries are at $z = 0$ and $z = L$, where L is the sample thickness. This symmetry allows us to solve $W_\perp(x, y, t)$ by using its two-dimensional spatial Fourier transform $W_\perp(\mathbf{q}_\perp, t)$. Solving the (x, y)-part of Eq. (1) and using the initial condition $t = 0$ gives

$$W_\perp(\mathbf{q}_\perp, t) = W(\mathbf{q}_\perp, t = 0)\, e^{-Dq_\perp^2 t}\,. \tag{3}$$

Optics EXPRESS

Next we solve the remaining 1D equation

$$\frac{\partial W(z,t)}{\partial t} = D\frac{\partial^2 W(z,t)}{\partial z^2} \tag{4}$$

We will turn Eq. (4) into a Sturm-Liouville eigenvalue problem by introducing the Ansatz $W(z,t) = e^{-\gamma t}W(z)$

$$\frac{\partial^2 W(z)}{\partial z^2} + \grave{} W(z) = 0\,, \tag{5}$$

$$\grave{} \equiv \frac{\gamma}{D}\,. \tag{6}$$

As is well-known from linear algebra [48] solutions of Sturm-Liouville equations are orthogonal and form a complete set. To solve Eq. (5), we apply the Neumann's boundary conditions, which are given as

$$W(z=0) - z_{e1}\frac{\partial W(z)}{\partial z}\Big|_{z=0} = 0 \tag{7}$$

and

$$W(z=L) + z_{e2}\frac{\partial W(z)}{\partial z}\Big|_{z=L} = 0\,, \tag{8}$$

where z_{e1} and z_{e2} are extrapolation lengths at the front and back surfaces of the sample respectively. Applying the boundary conditions in Eqs. 7 and 8 will lead to a discrete set of eigenvalues $\grave{}_m$. The general eigenfunction for eigenvalue $\grave{}_m$ can be cast in the form

$$W_m(z) = A_m^{-1/2}\sin(\kappa_m z + \eta_m)\,. \tag{9}$$

As outlined in detail in [55] the wavevector κ_m and phase η_m will be determined from solving Eq. (5) with the boundary conditions. The parameter A_m takes care of the normalization of the eigenfunctions, such that

$$\int_0^L W_m W_n\, dz = \delta_{mn}, \tag{10}$$

where δ_{mn} is the Kronecker delta. The relation between the eigenvalue and wavevector is $\grave{}_m = D\kappa_m^2$. The allowed wave vectors κ_m are obtained by solving the implicit equation

$$\tan(\kappa_m L) = \frac{(z_{e1}+z_{e2})\kappa_m}{z_{e1}z_{e2}\kappa_m^2 - 1}\,. \tag{11}$$

Following [55], the phase factor η_m fulfills the following equation [56]

$$\tan\eta_m = z_{e1}\kappa_m\,, \tag{12}$$

and the normalization factor A_m is given by

$$A_m = \frac{1}{2}L - \frac{1}{2\kappa_m}\cos(\kappa_m L + 2\eta_m)\sin(\kappa_m L)\,. \tag{13}$$

For the exact solution of Eq. (11), see Appendix. The first ten wavevectors obtained from the solution are shown in Table **1** for a particular set of boundary conditions. In Fig. 1, we plot the first three eigenfunctions using Eq. (9) with the same set of boundary conditions. The fundamental diffusion eigenfunction $m = 1$ is a half-period sine function, which has positive values throughout the sample. Therefore, the $m = 1$ eigenfunction can describe a specific energy density inside a scattering medium, since the energy density is positive. On the other hand, the

Optics EXPRESS

Table 1. Wavevectors[a] κ_m for the First 10 Eigenfunctions of the Diffusion Equation.

Eigenfunction index m	Wavevector κ_m
1	0.229566
2	0.460711
3	0.694591
4	0.931747
5	1.172199
6	1.415643
7	1.661649
8	1.909776
9	2.159633
10	2.410889

[a] The values were obtained by solving Eq. (11). The extrapolation lengths are $z_{e1} = z_{e2} = z_e\ell = (\pi/4)\ell$ (for a 2D sample [4]) and L = 12.1ℓ.

$m = 2$ and $m = 3$ diffusion eigenfunctions (and other higher eigenfunctions not shown) have both positive and negative values within the sample boundary. Since a negative energy density is non-physical, diffusion eigenfunctions $m = 2$ and $m = 3$ cannot *individually* describe energy density inside a scattering medium. However, a sum over these diffusion eigensolutions that yields positive values throughout the sample can describe a physical energy density inside the medium. The weight of the fundamental eigenfunction takes care of the sum to be positive everywhere.

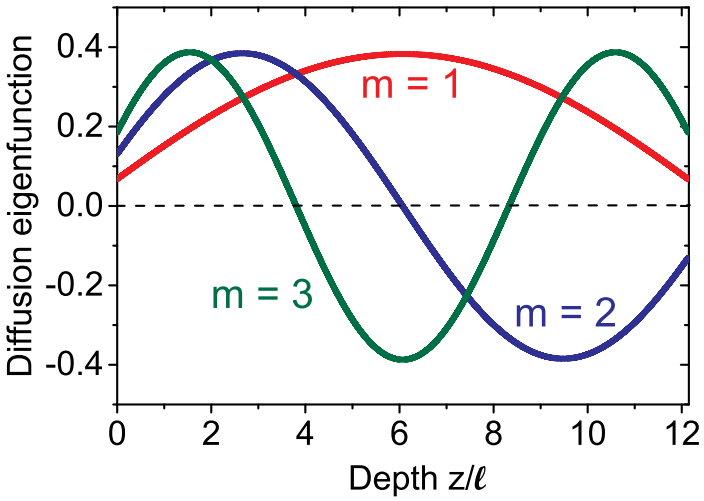

Fig. 1. The first three eigenfunctions of the diffusion equation plotted using equation Eq. (9). The wave vectors κ_m are presented in table **1** and the used parameters can be found in the caption of that table.

Optics EXPRESS

2.2. Reconstructing the energy density with eigenfunctions of the diffusion equation

The diffusion equation is of the Sturm-Liouville type so its eigenfunctions form a complete and orthogonal set [48]. Therefore, any distribution of energy density within the domain of the sample boundaries can be decomposed into a sum over a finite number M of eigenfunctions for a specific set of coefficients. Such a decomposition is only useful if the number of needed modes is small. We express a certain ensemble averaged energy density $W_s(z)$ inside the scattering medium in terms of the normalized eigenfunctions $W_m(z)$

$$W_s(z) = \sum_{m=1}^{M} d_m W_m(z)\,, \tag{14}$$

where d_m are coefficients. We calculate the overlap integral I_p of the product of $W_s(z)$ and $W_p(z)$

$$I_p \equiv \int_{z=0}^{z=L} dz\, W_s(z) W_p(z)\,, \tag{15}$$

and substitute Eq. (14) into Eq. (15) to obtain

$$I_p = \int_{z=0}^{z=L} dz \sum_{m=1}^{M} d_m W_m(z) W_p(z)\,. \tag{16}$$

We use the orthonormality of functions $W_p(z)$ and $W_m(z)$, which is expressed as

$$\int_{z=0}^{z=L} dz\, W_p(z) W_m(z) = \delta_{mp}\,, \tag{17}$$

Therefore, Eq. (16) becomes

$$I_p = \sum_{m=1}^{M} d_m \delta_{mp} = d_p\,. \tag{18}$$

We now can write the decomposition (14) as

$$W_s(z) = \sum_{m=1}^{M} I_m W_m(z)\,, \tag{19}$$

In this paper, the spatial energy density $W_s(z)$ that we reconstruct is that of shaped waves $W_{\mathrm{sw}}(z)$. We also reconstruct the spatial energy density of transmission eigenchannels $W_n(z,\tau)$. The spatial energy densities are obtained from numerical simulation and the details of the simulation are described in Section 3. The simulation results are compared to the reconstructed energy density $W_{\mathrm{re}}(z)$ in Section 4.

In order to quantify the overlap between the reconstructed function $W_{\mathrm{re}}(z)$ and the numerical data $W_s(z)$, we use the cosine distance COSD [57], which is defined as

$$\mathrm{COSD} \equiv 1 - \frac{\sum_{\mathrm{i}=1}^{\mathrm{N_s}} \mathrm{W_{re}(z_i) W_s(z_i)}}{[\sum_{\mathrm{i}=1}^{\mathrm{N_s}} \mathrm{W_{re}^2(z_i)}]^{\frac{1}{2}} [\sum_{\mathrm{i}=1}^{\mathrm{N_s}} \mathrm{W_s^2(z_i)}]^{\frac{1}{2}}}\,. \tag{20}$$

N_s is the number of points in the simulation data. COSD varies between 1 and 0 and tends towards 0 as the reconstructed function fully describes the simulation data. As a figure-of-merit of a good reconstruction, we choose the eigenfunction that has COSD $\leq 10^{-4}$. At this COSD, the reconstructed function deviates by only 2% from the actual function. This level of accuracy is within what is achievable in a measurement with a realistic level of experimental noise.

Optics EXPRESS

3. Numerical samples and setup

3.1. Numerical setup

We perform simulations of transport of monochromatic scalar waves through a waveguide containing scatterers. The waveguide is modeled as a quasi-one-dimensional (quasi-1D) system possessing $N_m = 100$ transversal modes, with elastic scattering on bulk impurities. This is implemented as a 2D waveguide with 100 transversal modes, containing scatterers at random positions with a density of 0.2 scatterer per square wavelength. A schematic of the numerical sample is shown in Fig. 2. In order to calculate the energy density inside the waveguide we

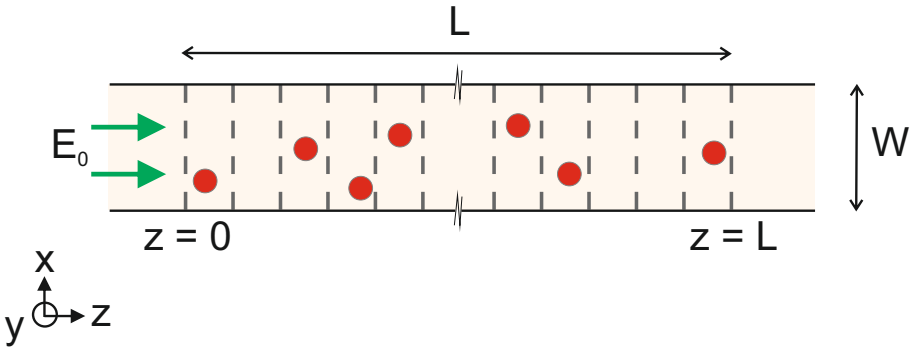

Fig. 2. Schematic of the numerical sample: a quasi-1D waveguide. In the region $z = 0$ to $z = L$, scatterers (red cirles) are randomly distributed in the waveguide. The width W and length L of the scattering part of the waveguide are such that $W \ll L$. The waveguide is illuminated with an incident field E_0 that is scattered in the waveguide. The waveguide is divided into slices (vertical dashed line) and in each slice there is at most one scattering particle. The scattering matrix of each of the slices is computed and concatenated to give the scattering matrix of the whole sample.

employ a recursive S-matrix formalism, where the waveguide is first divided into sub-wavelength slices, each containing a maximum of one scatterer. For each slice we define the S-matrix in a mode representation as follows [53],

$$S = \begin{pmatrix} R_L & T^T \\ T & R_R \end{pmatrix}, \tag{21}$$

where R_L and R_R are the left and right reflection matrix respectively of dimension $N_m \times N_m$, T is the left-to-right transmission matrix. The right-to-left transmission matrix in this reciprocal system is the transpose of T. The S-matrix of each slice, of dimensions $2N_m \times 2N_m$, is calculated in the approximation that no recurrent scattering takes place within the thin slice. Next, the S-matrices of the slices are joined, including contributions of recurrent scattering, using the composition rule for S-matrices [51]. This numerically stable procedure yields the S-matrix of the entire waveguide and of subsections of it. From the transmission matrix we extract the singular values and vectors corresponding to all channels by singular value decomposition. The energy density inside the waveguide, for a given incident field, is calculated as follows: For a given axial coordinate z_c the S matrices S_1,S_2 of the waveguide sections $0 < z < z_c$ and $z_c < z < L$ respectively are calculated. The field in the $z = z_c$ plane is then found by calculating recurrent scattering diagrams:

$$E_c = T_1 E_{in} + R_{L2} T_1 E_{in} + R_{R1} R_{L2} T_1 E_{in} + R_{L2} R_{R1} R_{L2} T_1 E_{in} + \ldots \tag{22}$$

Optics EXPRESS

$$= (1 + R_{L2})(1 - R_{R1}R_{L2})^{-1}T_1E_{in}. \quad (23)$$

Here, R_{L2} is the left reflection submatrix of S_2, R_{R1} is the right reflection submatrix of S_1, and T_1 is the left to right transmission submatrix of S_1. Subsequently for every z_s the time-averaged energy density $\varepsilon_0|E_c|^2$ is integrated over the cross section to obtain the projected energy density $W(z)$. The calculation is repeated for 8000 independently generated random waveguides from which the transmission channels are extracted. To obtain plots of the average energy density as a function of transmission, we average the energy densities of channels in a narrow band of transmission values.

3.2. Sample characterization

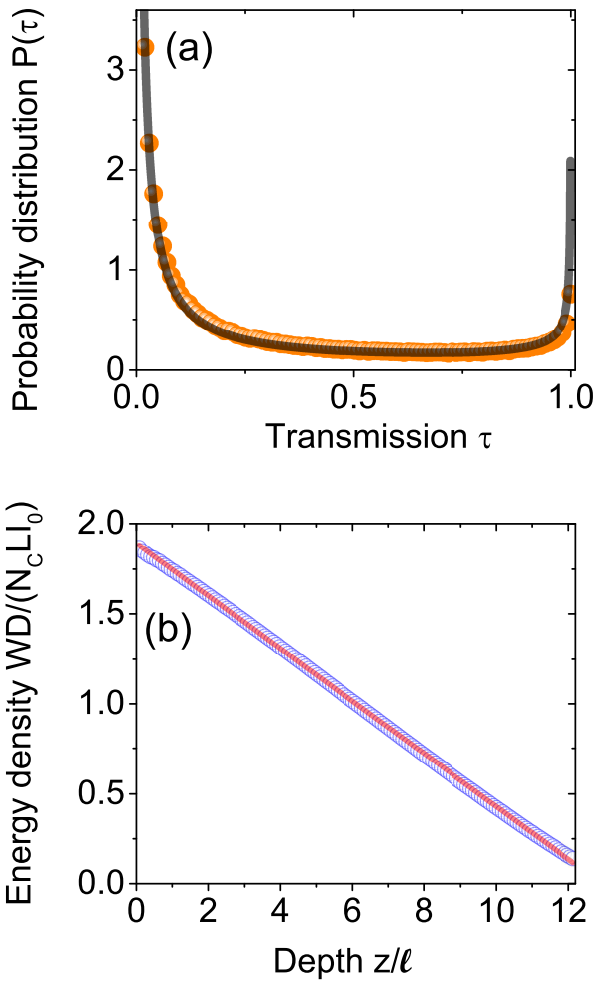

Fig. 3. (a) Probability distribution of the transmission from the simulation (blue dots) and the expected Dorokhov-Mello-Pereyra-Kumar (DMPK) distribution (red curve). (b) An equally-weighted summation over the energy density of all transmission channels (blue dots) and the expectation from diffusion theory (red line) as a function of the normalized depth z/ℓ. In (a) and (b), we ensemble averaged over 8000 waveguides and the sample thickness is $L = 12.1\ell$.

Optics EXPRESS

In order to characterize the numerical samples, we plot in Fig. 3(a) the probability distribution $P(\tau)$ as a function of the transmission τ. The probability distribution $P(\tau)$ obtained from the simulation is bi-modal: there is a high probability for transmitting channels with transmission τ close to zero and close to one. In Fig. 3(a), we compare the Dorokhov-Mello-Pereyra-Kumar (DMPK) distribution [53] with our numerical result. The probability distribution of transmission for a scattering medium is expected to follow the DMPK distribution. Indeed, the DMPK distribution agrees well with our numerical result. Furthermore, in order to confirm that our numerical samples are in the diffusive regime, we plot in Fig. 3(b) the equally-weighted ensemble averaged energy density versus reduced sample depth. The ensemble averaged energy density shows a linear decrease from the front surface towards the end surface of the sample, in agreement with the prediction of diffusion theory for a diffusive sample, see Fig. 3(b).

4. Results and discussions

4.1. Energy density of shaped waves

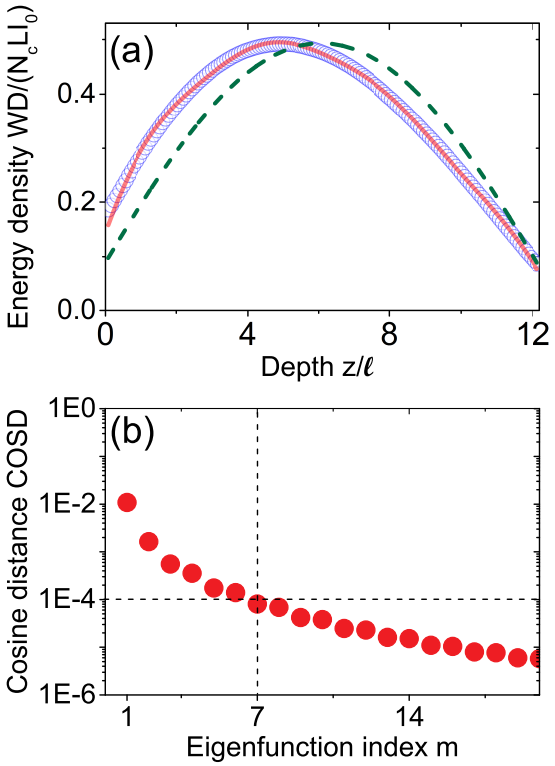

Fig. 4. (a) Transmission-weighted averaged energy density versus normalized sample depth z/ℓ. The transmission-weighted averaged energy density is equivalent to wavefront-shaped or phase-conjugated light [7]. The blue circles are the energy density obtained from simulation, the green line is the diffusion $m = 1$ eigenfunction, and the red line is the summation over the first seven eigenfunctions. (b) Cosine distance COSD versus eigenfunction index m. The vertical and horizontal dashed-lines shows the position of our figure-of-merit COSD $\approx 10^{-4}$ and the eigenfunctions that fulfill the criterion $m = 7$ respectively. In both (a) and (b), the sample is the same as in Fig. 3.

Optics EXPRESS

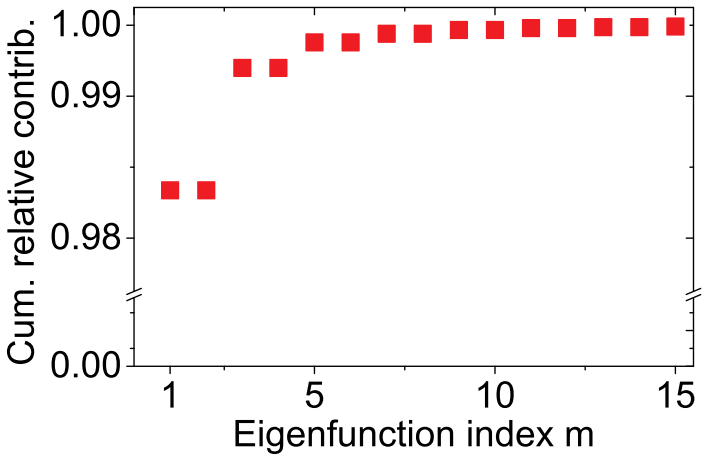

Fig. 5. The cumulative contribution of the eigenfunctions of the diffusion equation to the total internal energy density of shaped waves relative to a sum over the first 100 eigenfunctions versus the eigenfunction index m.

We obtained the energy density of shaped waves W_{sw} as the transmission-weighted ensemble average of the energy density of transmission channels $W_n(z,\tau)$, as shown in [7, 11]:

$$W_{\mathrm{sw}}(z) = \sum_{n}^{N} \tau_n W_n(z,\tau)\,, \tag{24}$$

where N is the number of transmission channels. Eq. (24) implies that wavefront shaping couples an energy fraction of exactly τ_n into a transmission eigenchannel n. Using Eq. (24), we obtained the energy density of the shaped waves from the transmission-weighted average over the energy density of all transmission channels. We show in Fig. 4(a) the ensemble averaged energy density distribution of shaped waves. The energy density distribution of the shaped waves increases from the interfaces of the sample and is maximal at $z = 4.9\ell$, which is about 20% off the center of the sample ($z = 6.1\ell$). The ensemble averaged energy density of wavefront-shaped light was first obtain in [43] by solving the Maxwell equation using the finite-difference time-domain (FDTD) method. Despite the different numerical calculation methods, our numerical result is closely similar to the one obtained by Choi *et al* [43]. The exact peak position of the energy density obtained in [43] is difficult to estimate due to the noise in the data, however, the peak position is close to the center of the sample.

We reconstructed the distribution of the energy density of shaped waves from eigenfunctions of the diffusion equation. From the reconstruction, we obtain the cosine distance COSD, which we plot in Fig. 4. In case of shaped waves, a summation over the first $M = 7$ eigenfunctions is remarkably sufficient (COSD $\leq 10^{-4}$) to reconstruct the energy density, see Fig. 4(a). Only the fundamental diffusion eigenfunction $m = 1$ has COSD $\approx 10^{-2}$ and is not sufficient to describe the energy density profile. The fundamental eigensolution peaks at exactly the center of the sample, in contrast to the energy density of shaped waves. To put the number $M = 7$ in perspective, we performed the same reconstruction on the profile of 50 speckle spots within the same sample domain. We find that over 300 eigenfunctions are required to obtain a COSD $\leq 10^{-4}$, indicating that the diffusion eigenfunctions are not a suitable basis for a random speckle. In contrast, the low number of eigenfunctions required to represent the shaped waves implies that the solution of the diffusion equation is close to the ensemble averaged energy density of shaped waves.

We further investigated the contribution of the eigenfunctions to the *total* energy density

Optics EXPRESS

integrated along the depth of the sample relative to the contribution of the first 100 eigenfunctions. As a reference, we choose the first 100 eigenfunctions because the higher order eigenfunctions have a very negligible contribution. In Fig. 5, we plot the contributions. For shaped waves, the $m = 1$ contributes 98% of the *total* energy density inside the sample. Remarkably, our finding about the strong contribution of $m = 1$ to the total internal energy density agrees very well with the heuristic model in [47] that wavefront shaping *predominantly* couples light to the fundamental diffusion eigensolution. The contribution of $m = 2$ is negligible compared to $m = 1$ since $m = 2$ has negative energy density in almost half of the sample depth, which cancels the positive energy density (see Fig. 1). A similar effect also happens for all other even index eigenfunction.

4.2. Energy density of transmission channels

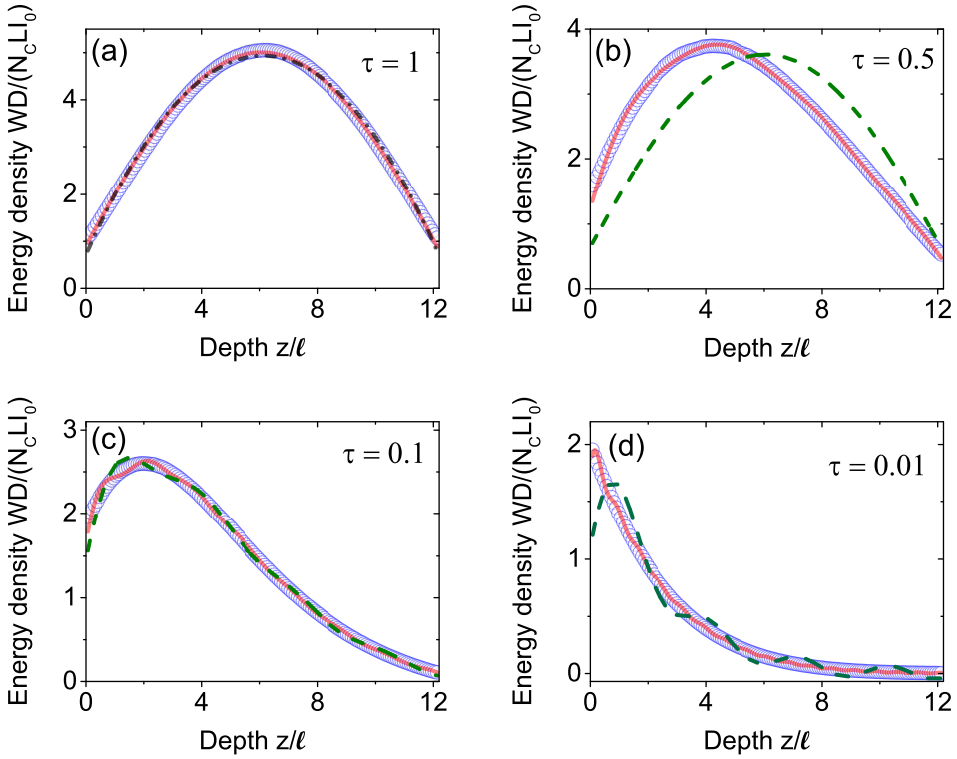

Fig. 6. (a) Ensemble averaged energy density of an open channel in a scattering medium versus normalized depth z/l_{tr} with transmission τ in the range $0.99 < \tau < 1$. The blue circles are the energy density data obtained from simulation, and the red line is the fundamental diffusion eigenfunction $m = 1$. The black dashed-dotted curve is a parabolic fit. (b) Ensemble averaged energy density of transmission channels in a scattering medium versus the normalized depth z/l_{tr} for transmission τ in the range $0.49 < \tau < 0.51$. The blue circles are the energy density data obtained from simulation, the green line is the diffusion $m = 1$ eigenfunction, and the red line is a $M = 7$ summation of diffusion eigenfunctions. (c) The blue circles are obtained as in (a) and the transmission τ is in the range of $0.09 < \tau < 0.11$. The green and the red lines are summations over $M = 8$ and $M = 16$ diffusion eigenfunctions respectively. (d) The blue circles are obtained as in (a) and the transmission τ is in the range: $0 < \tau < 0.02$, which signifies closed channels. The green and the red lines are summations over $M = 8$ and $M = 33$ diffusion eigenfunction respectively.

Optics EXPRESS

The ensemble averaged energy density of open transmitting eigenchannels with a transmission τ in the range $0.99 < \tau < 1$ is shown in Fig. 6. The energy density shows a symmetric profile, which peaks in the middle of the sample. Our numerical result is similar to the one obtained by Davy *et al* [44]. Interestingly, only the fundamental diffusion eigenfunction $m = 1$ is sufficient to reconstruct the energy density of the open channel, see Fig. 4(a). The fundamental diffusion eigenfunction $m = 1$ is expected to describe the open eigenchannels for the following reasons: Firstly, as the open eigenchannel has the highest individual transmission, the fundamental eigenfunction ($m = 1$) as well contributes most to the total transmission as shown in [47]. Secondly, the fundamental eigenfunction is the only physical solution with a positive energy density along the sample depth z, see Fig. 1 and therefore this eigenfunction must have the largest weight in the expansion. Interestingly, a simplified mathematical model by Davy *et al* [44] described the energy density of open channels as a parabolic function. We note that the deviations from a parabolic shape are obvious only near the edges, and the shape of the energy density curve agrees better with the cosine shape of the fundamental eigenfunction, see Fig. 6(a). Indeed, the COSD for the parabola is 10^{-3} compared to 10^{-5} for the fundamental eigenfunction.

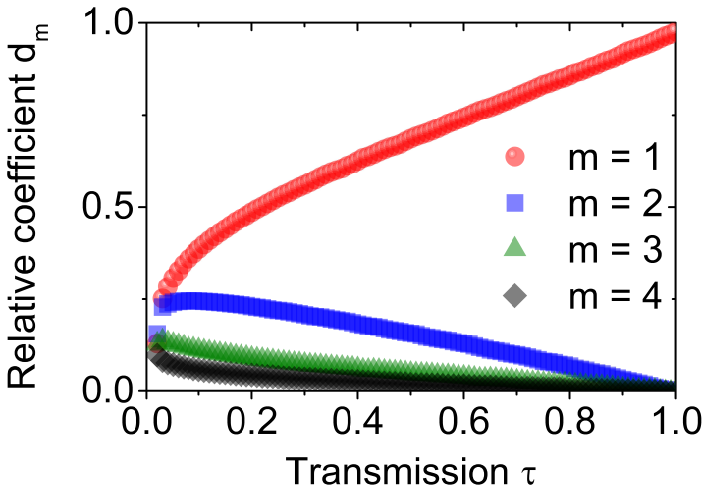

Fig. 7. Contribution of eigenfunctions of the diffusion equation relative to a sum of the first 100 eigenfunctions versus transmission τ for eigenfunctions $m = 1, 2, 3$, and 4 plotted with red circles, blue squares, green triangles, and black diamonds respectively.

We also use the eigenfunctions of the diffusion equation to reconstruct the ensemble averaged energy densities of low-transmission channels obtained from simulation. In Figs. 6 (b - d), we show the ensemble averaged energy densities for transmission eigenchannels with transmissions $\tau = 0.5$, 0.10 and 0.01. For the eigenchannel with transmission $\tau = 0.5$, only $M = 7$ eigenfunctions of the diffusion equation are sufficient to reconstruct its energy density, $M = 16$ eigenfunctions for $\tau = 0.1$, and $M = 33$ is required for a closed channel $\tau = 0.01$. As the transmission τ decreases, the number of eigenfunctions sufficient to reconstruct the energy density increases. The increase in the number M of sufficient eigenfunctions is because the asymmetry of the distribution of energy density increases as the transmission τ reduces, and likewise, the asymmetry of the eigenfunctions increases with the eigensolution index. Therefore, the higher index eigenfunctions contribute more to an asymmetric function. The contribution of the eigenfunctions with index $m = 1$, 2, 3 and 4 relative to a summation over the first 100 eigenfunctions is shown in Fig. 7. The relative contribution of the fundamental eigenfunction

Optics EXPRESS

of the diffusion equation $m = 1$, which is a symmetric function, increases as the transmission increases, while the relative contributions of the greater index eigenfunctions, which are asymmetric functions, are higher for low-transmission channels. In Ref. [44], Davy *et al.* obtained the energy density of the transmission eigenchannels using a numerical method that is similar to ours. The authors describe the profile of the transmission eigenchannels with the solution of an implicit equation. In contrast, our approach provides accurate heuristic analytical expressions that describe the profile of the transmission eigenchannels, which constitutes a complementary approach.

4.3. Effect of sample thickness

Here, we investigate the effect of the sample thickness on the number of eigenfunctions sufficient to reconstruct the energy density of shaped waves. We therefore perform simulations of the energy density on different samples with a range of sample thicknesses: $L = 5\ell, 12.1\ell, 18.8\ell$ and 39.5ℓ. We show in Fig. 8 the COSD versus the eigensolution index for the 4 samples. Interestingly, all the samples have a convergence to a value of COSD $\leq 10^{-4}$ at the seventh eigensolution. There is a slight deviation for the thickest sample $L = 39.5\ell$ that is probably due to artifacts from the simulation due to the large number of waveguide slices. This convergence of the COSD shows that the summation over the first 7 eigenfunctions of the diffusion equation is sufficient to describe the energy density of shaped waves, *irrespective* of the sample thickness.

In the previous sections, we have seen that the diffusion fundamental eigenfunction of the diffusion equation $m = 1$ dominates the energy density of high-transmission channels. We investigate if this result holds for the different samples thicknesses. In Fig. 8, we show the coefficient of the $m = 1$ mode relative to the sum of the first 100 eigenfunctions versus the transmission for the 4 different thicknesses. The relative contribution of the $m = 1$ mode is similar for all samples, irrespective of the thickness and this is quite remarkable. The fundamental diffusion eigenfunction dominates the energy density of high-transmission channels for all sample thicknesses.

5. Conclusion

We have shown that only a few eigenfunctions of the diffusion equation suffice to accurately reconstruct the distribution of the shaped energy density inside a quasi-1D scattering waveguides. In particular, the fundamental eigenfunction of the diffusion equation is very similar to the distribution of energy density of shaped waves. To reconstruct the distribution of open channels only the diffusion fundamental eigenfunction $m = 1$ is sufficient. In addition, we have shown that a few diffusion eigenfunctions reconstruct the energy density of low-transmission eigenchannels, to a great precision. The diffusion eigenfunctions are very efficient to reconstruct these energy densities that are within the boundaries of the sample. This reconstruction is enlightening because even energy densities that are as a result of wave phenomena – shaped waves and transmission eigenchannels – can be described efficiently with diffusion eigenfunctions. The diffusion eigenfunctions are capable of this reconstruction since they are a complete set of functions. Our results are relevant for applications that require the precise knowledge of distribution of the energy density inside scattering media. Such applications include efficient light harvesting in solar cells especially in near infrared where silicon has a low absorption [37–39]; enhanced energy conversion in white LEDs, which serves to reduce the quantity of expensive phosphor [32–36]; low threshold and higher output yield of random lasers [40, 41]; as well as in homogeneous excitation of probes in biological tissues [42].

Optics EXPRESS

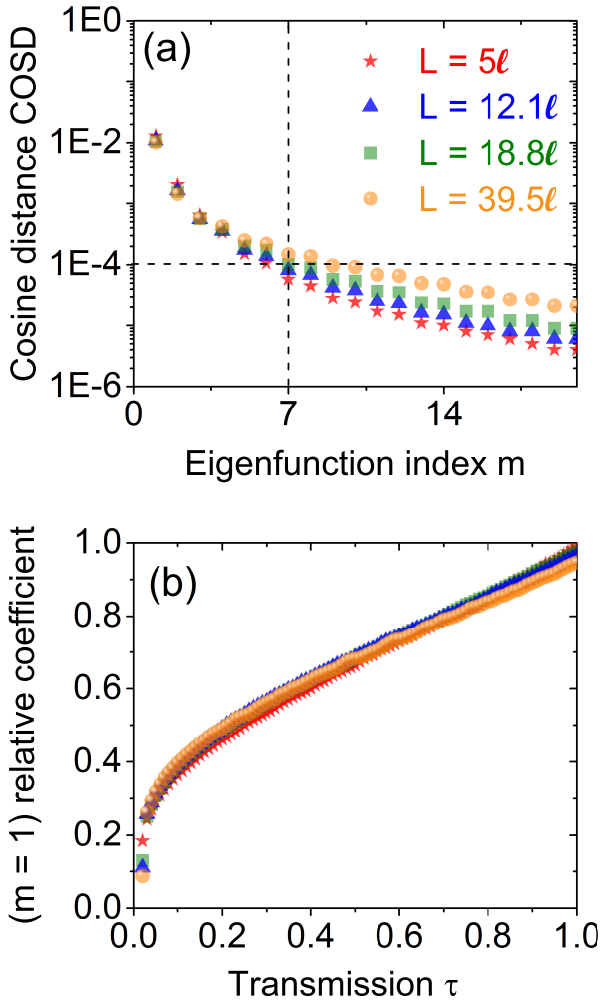

Fig. 8. (a) Cosine distance COSD versus eigenfunction index m for 4 samples with different thickness: $L = 5\ell, 12.1\ell, 18.8\ell$ and 39.5ℓ, which are plotted as pink stars, green squares, blue triangles, and orange circles respectively. The vertical and horizontal dashed-lines shows position of our figure-of-merit COSD $\approx 10^{-4}$ and the eigenfunction, which fulfills the criterion $m = 7$ respectively. (b) Contribution of the fundamental diffusion mode $m = 1$ relative to the sum of the first 100 eigenfunctions as a function of transmission τ.

A. Method of calculating the wave vectors of diffusion eigenfunctions

In Eq. (11), we show an implicit equation, which defines the allowed wave vectors of the diffusion eigenfunctions. The equation is again stated here:

$$\tan(\kappa_m L) = \frac{(z_{e1} + z_{e2})\kappa_m}{z_{e1} z_{e2} \kappa_m^2 - 1}. \tag{25}$$

We define

$$f(\kappa_m) = f_1(\kappa_m) - f_2(\kappa_m), \tag{26}$$

Optics EXPRESS

where

$$f_1(\kappa_m) \equiv \tan(\kappa_m L) \tag{27}$$

and

$$f_2(\kappa_m) \equiv \frac{(z_{e1} + z_{e2})\kappa_m}{z_{e1} z_{e2} \kappa_m^2 - 1} . \tag{28}$$

Our goal is to find the wave vectors κ_m^{r} that fulfills the condition

$$f(\kappa_m^{\mathrm{r}}) = 0 . \tag{29}$$

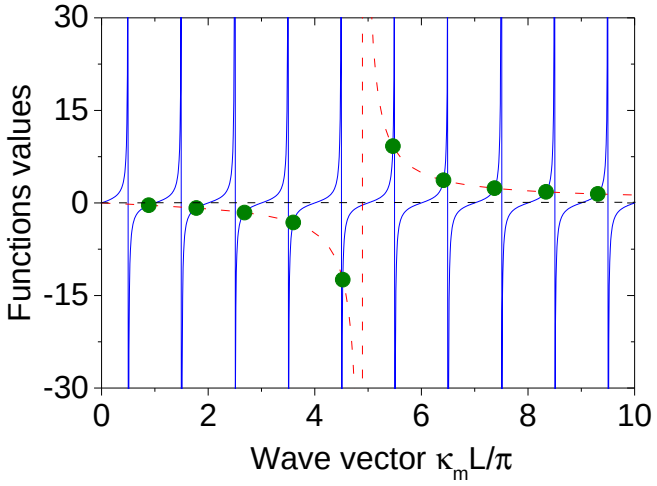

Fig. 9. The values of functions f_1 (blue line) and f_2 (red dashed line) in Eqs. 27 and 28. as a function of reduced diffusion wave vector $\kappa_m L/\pi$. The green circles are the roots of Eq. 25.

In Fig. 9, we plot the two functions f_1 and f_2. The condition in Eq. (29) is fulfilled by the wave vectors κ_m^{r} at the intersection of the two functions f_1 and f_2, as indicated in Fig. 9. We found the wave vectors κ_m^{r} by dividing function f into domains with size π/L. In most of the domains, only one root is expected, except the domain where the function f_2 has a divergence, where two roots appear. In each domain, we use a Simple Bisection method to search the domain for wave vectors that fulfill the desired condition. Each domain is divided into two equal parts. The function f is first evaluated for the left part of the domain and then checked if there is any root present. If there is no root present, the left domain is further divided into smaller subdomains and each subdomains is searched for the root. We divide the domains until the size of the subdomain is 10^{-12}. If there is no root in all the subdomains of the left domain, then, the right domain is searched. This way, all the desired roots are found iteratively.

Acknowledgment

We thank Pepijn Pinkse, Henri Thyrrestrup, Hasan Yilmaz, and Hui Cao for useful discussions. This project is part of the research program of the "Stichting voor Fundamenteel Onderzoek der Materie" (FOM) FOM-program "Stirring of light!", which is part of the "Nederlandse Organisatie voor Wetenschappelijk Onderzoek" (NWO). We acknowledge NWO-Vici, DARPA, ERC grants 279248, 678919, and STW.